Seismic response of concrete arch dams due to different non-uniform ground motion models

M. Dehghani[*], *H. Mirzabozorg*[**], *S.M. Aghajanzadeh*[***]

Abstract:

This paper investigates the effects of spatially variable (non-uniform) seismic excitation incorporating incoherency effect on earthquake-induced stresses of arch dams. Coherency functions reflect the waveform variation between two different stations, which decays with an increment of distance and frequency. The response spectrum compatible non-uniform ground motions are generated utilizing the coherency functions. Besides, to study the valley shape effects and dam height on seismic responses, V-shaped and U- shaped valleys with different heights are considered. Finite element models of typical arch dams are provided, including the relevant compressible reservoirs and surrounding massed foundation rocks. Dynamic analyses are carried out for uniform and non-uniform excitations. Comparing the stress magnitudes revealed that, non-uniform ground motion inputs considering coherency functions lead to less tensile and compressive stresses than the uniform ones(identical excitation across the supports). Moreover, the stress distribution pattern depends on the utilized coherency function. Finally, the results demonstrated that the magnitude of maximum tensile stress is lower in the V-shaped valley as a general trend. Additionally, due to uniform excitation, the increase of dam height leads to an increment of tensile stresses.

1. Introduction

A proper seismic analysis of arch dams as large infrastructures is one of the challenging engineering issues. Several methods have been presented to analyze the response of dams by focusing on ground motions effects to investigate the probable failure modes of the dam[1]. In conventional methods, in the analysis and design stage, a dam is excited uniformly along with the abutments. However, it may undergo variable excitation along with their supports on account of Spatial Variation of Earthquake Ground Motions (SVEGM), which stands for changes in the characteristic of excitations due to its extended interface with the earth. Spatially varying motions are non-uniform (multiple) and asynchronous.

The first term (non-uniform) refers to the changes in amplitude and phases of the waves, and the asynchronous describes the delay in the arrival of the waves due to the limited speed of the waves[2]. The main causes of SVEGM are the wave passage effect, incoherence, and the local site condition[3]. During the last few decades, substantial attention has been paid to the dynamic analysis of structures considering spatially varying inputs. It has been demonstrated that the dynamic analysis using one identical excitation along all supports of an extended structure (conventional methods) yields unrealistic results[4]. This is because, the response of structures to SVEGMs comprises of two main components: quasi-static and dynamic responses[5] The dynamic responses result from inertia, while the quasi-static response is caused by the comparative transposition of the excitation points toward uniform excitations, as the non-uniform excitations lead to quasi-static responses [6]. That is, while the quasi-static is a rigid

_____

* Graduate Student, Department of Civil Engineering, K.N. Toosi University of Technology, Tehran, Iran
** Corresponding author: Associate Professor, Department of Civil Engineering, K.N. Toosi University of Technology, Tehran, Iran. Email: mirzabozorg@kntu.ac.ir
*** Graduate PhD Student, Department of Civil Engineering, K.N. Toosi University of Technology, Tehran, Iran.

component under uniform excitation, it induces relative displacement through a non-uniform one[7]. It has been declared that SVEGM's effect on the responses of the dam significantly depends on the ratio of quasi-static elements.[4] Mirzabozorg et al. [8] studied the effect of non-uniform excitation on a double curvature arch dam. They demonstrate that non-uniform excitations give rise to smaller responses. This result has been justified on the basis of other studies[9, 10]. In some cases, non-uniform excitations have generated greater responses[11, 12]. Other researchers reported that the incremental or subtractive impact of differential excitation could vary depending on the response type like the stress, displacement, hydraulic pressure, etc.[2, 13]. These discrepancies are due to the structural modeling methodology, simulated ground motion, and other research hypotheses [14, 15]. Selection of a coherency model, apparent wave velocity, local site condition, rotational ground motion, soil-structure interaction, and boundary conditions are sources of uncertainty[15]. The main conclusion drawn from related researches is that the effect of SVEGM on the responses of extended structures is poorly predictable due to all related uncertainties, and further comprehensive exploration is required to better understand the behavior of a dam through a non-uniform excitation.

The effect of wave passage has advanced in a group of studies. The influence of asynchronous earthquake motions on the response of a concrete gravity dam was explored by applying different wave passage velocities through research by Huang and Zerva [6]. They indicated that the responses increase with decreasing wave velocities and the slowest wave velocity produces the greatest response. Moreover, slow waves causes the most intense damages in the dam body. Similar conclusions have been drawn in other investigations, like [16-20] confirming the significance of wave passage effect on the response of long structures.

Spatially varying earthquake ground motions are mainly characterized by coherency functions. These functions describe the degree of difference between excitations at two distanced stations. Analyzing the influence of coherency has manifested the sensitivity of responses to coherency and the significance of exploring the effects of different coherency functions on structures' responses due to non-uniform excitation [9, 14]. Chen and Harichandran [21] used a 3D model of an earth dam to analyze the effect of SEVGM on the dam response. They revealed that using coherency functions, which diminish rapidly with space, yield large shear stresses at the dam body's base. Despite the significance of selecting a proper coherency function and its pertinent parameters, there are very few categories of research on this subject, and it is still an open issue. Modeling of spatially varying earthquake ground motion is important and challenging. Thus, various methods have been

proposed for simulating spatially varying earthquake ground motions [22-26]. Deodatis [23] introduced an iterative scheme to generate seismic ground motion time histories based on some recorded ground motions at different locations compatible with the prescribed response spectra. Wang et al. [26] extracted the non-stationary frequency information from recorded data. Cacciola and Deodatis [22] proposed a method for generating a fully non-stationary and spectrum-compatible earthquake ground motion vector process based on the spectral representation method.

This study focuses on the effects of coherency functions on linear dynamic responses of a series of typical concrete arch dams. Fully non-stationary and spectrum-compatible ground motions are generated utilizing the algorithm proposed by Cacciola and Deodatis [22] in section 2. The generated ground motions are target response spectrum-compatible. Harichandran-Vanmarcke and HindyNovak models are chosen as the coherency functions. Then, the generated uniform and non-uniform ground motions are applied to the V-shaped/U-shaped valley models of typical dams comprising of 250m and 150m heights in section 3. Modeling several dam body shapes and investigating the effect of various parameters like valley shape and the height of the dam body besides and the effects of coherency functions is the novelty of the current work. Results are presented and interpreted in section 4. Subsequently, concluding remarks are reported in the last section (see section 5).

2. Simulation of SVEGM

In this study, the fully non-stationary, spectrum-compatible ground motion vector processes are generated using the algorithm proposed by Cacciola and Deodatis[22].

In the utilized algorithm, the ground motion vector process is generated by the superposition of the two components' power spectral density: the local component and the corrective term. The local component $(f_j^L(t), \ (j = 1, 2, ..., m))$ considers the non-stationary and spatial variation related to the site, and the corrective term $(f_j^C(t), \ (j = 1, 2, ..., m))$ makes the local component spectrum-compatible.

2.1 Local Component

The local component is a fully non-stationary vector process, which means that both the amplitude and frequency contents of the ground motion change as a function of time. In this method(see details in[22]), the local component is modeled by evolutionary power spectral density, known as a non-separable non-stationary cross-spectral density matrix. Clough-Penzien spectrum[27] is selected to model the non-separable power spectral density functions given as:

$$S^L(\omega,t) = \begin{pmatrix} S_{11}^L(\omega,t) & S_{12}^L(\omega,t) & \cdots & S_{1m}^L(\omega,t) \\ S_{21}^L(\omega,t) & S_{22}^L(\omega,t) & \cdots & S_{2m}^L(\omega,t) \\ \vdots & \vdots & \ddots & \vdots \\ S_{31}^L(\omega,t) & S_{32}^L(\omega,t) & \cdots & S_{3m}^L(\omega,t) \end{pmatrix} \qquad (1)$$

The first step of computing Eq. (1) is to calculate the diagonal elements of the cross-spectral density matrix:

$$S_{jj}^L(\omega,t) = A(t)^2 S_0(t) \frac{\left(1+4\zeta_g^2(t)(\frac{\omega}{\omega_g(t)})^2\right)}{\left(1-(\frac{\omega}{\omega_g(t)})^2\right)^2 + 4\zeta_g^2(t)(\frac{\omega}{\omega_g(t)})^2} \times \frac{(\frac{\omega}{\omega_f(t)})^4}{\left(1-(\frac{\omega}{\omega_f(t)})^2\right)^2 + 4\zeta_f^2(t)(\frac{\omega}{\omega_f(t)})^2} \qquad (2)$$

where, $A(t)$ is the modulating function. The Bogdanoff-Goldberg-Bernard model [28] is selected for d for computing the modulating function:

$$A(t) = a_1 t \exp(-a_2 t); \qquad a_1 = 0.68s^{-1} \quad a_2 = \frac{1}{4}s^{-1} \qquad (3)$$

and, the intensity of the acceleration is:

$$S_0(t) = \frac{\sigma^2}{\pi\omega_g(t)(2\zeta_g(t) + \frac{1}{2\zeta_g(t)})}; \quad \sigma = 1m/s^2 \qquad (4)$$

In Eq. (4), the parameters $\omega_g(t)$ and $\zeta_g(t)$, $\omega_f(t)$ and $\zeta_f(t)$ are given in[29]:

The off-diagonal elements are obtained by multiplying the diagonal elements by the complex coherence function as following:

$$S_{jk}^L(\omega,t) = S_{jj}^L(\omega,t)\Gamma_{jk}(\omega) = S_{kk}^L(\omega,t)\Gamma_{jk}(\omega) \qquad (5)$$

$$\Gamma_{jk}(\omega) = \gamma_{jk}(\omega)\exp(-i\omega\xi_{jk}/v) \qquad (6)$$

where, ξ_{jk} is the distance between points j and k and; v is the apparent velocity of wave propagation. In Eq. (6), $\exp(-i\omega\xi_{jk}/v)$ describes the wave passage effect [30] and; $\gamma_{jk}(\omega)$ is the coherency function. The Harichandran-Vanmarcke [30] (see Eq. (7)) and Hindy-Novak [31] (see Eq. (8)) are chosen to describe the loss of coherency in the current study, given as:

$$\gamma_{jk}(\omega) = a\exp\left[-\frac{2\xi_{jk}}{\alpha\theta(\omega)}(1-a+\alpha a)\right] + (1-a)\exp\left[-\frac{2\xi_{jk}}{\theta(\omega)}(1-a+\alpha a)\right] \qquad (7)$$

$$a = 0.626 \quad \alpha = 0.022 \quad k = 19700m$$
$$\Omega = 12.692 rad/s \quad b = 3.47$$

$$\gamma_{jk}(\xi,\omega) = \exp\left[-(\alpha\xi\omega)^\beta\right] \qquad (8)$$
$$\alpha = 0.0778 \quad \beta = 0.31$$

The estimated evolutionary cross-spectral density matrix must be decomposed using Cholesky method at every time instant t to simulating the fully non-stationary vector process as following[32]:

$$S^L(\omega,t) = H(\omega,t)H^{T*}(\omega,t) \qquad (9)$$

Then, we have:

$$H(\omega,t) = \begin{bmatrix} H_{11}(\omega,t) & 0 & \cdots & 0 \\ H_{21}(\omega,t) & H_{22}(\omega,t) & \cdots & 0 \\ \vdots & \vdots & \ddots & \vdots \\ H_{m1}(\omega,t) & H_{m2}(\omega,t) & \cdots & H_{mm}(\omega,t) \end{bmatrix} \qquad (10)$$

Then, the fully non-stationary vector process of the local component $f_j^L(t)$, $(j=1,2,...,m)$ can be generated by the following series as $N \to \infty$:

$$f_j(t) = 2\sum_{r=1}^{m}\sum_{s=1}^{N}\left|H_{jr}(\omega_s,t)\right|\sqrt{\Delta\omega}\cos[\omega_s t - \vartheta_{jr}(\omega_s,t) + \phi_{rs}]; \quad j = 1,2,...,m \qquad (11)$$

$$\vartheta_{jk}(\omega_s,t) = \tan^{-1}\left|\frac{\text{Im}[H_{jk}(\omega,t)]}{\text{Re}[H_{jk}(\omega,t)]}\right| \qquad (12)$$

$$\omega_s = s\Delta\omega, \quad s = 1,2,...,N; \qquad \Delta\omega = \frac{\omega_c}{N} \qquad (13)$$

where, $\text{Im}[\bullet]$ and $\text{Re}[\bullet]$ denote the imaginary and real parts of a complex number, respectively, and ω_c represents an upper cut-off frequency. Beyond it, the element of the cross-spectral density matrix may be assumed to be zero at any time instant. Shinozuka and Deodatis [25] presented a criterion to estimate the value of ω_c. In addition, ϕ_{rs} $(r=1,2,....,m; \ s=1,2,...,N)$ are m sequences of N independent random phase angles distributed uniformly over the interval $[0,2\pi]$.

Now, the response spectrum should be calculated. To minimize the influence of the corrective term $(f_j^C(t))$ on the non-stationary characteristics of the corresponding term $(f_j^L(t))$, each component $(j=1,2,...,m)$ is scaled so its response spectrum $RSA^{f_j^L}(\omega)$ matches the corresponding target response spectrum $RSA^{(j)}(\omega)$ on at least one point. At the same time, the response spectrum of the local

component should be less than the target one at every frequency, which means $RSA^{f_j^L(t)}(\omega) \leq RSA^{(j)}(\omega)$.

2.2 Corrective Term

The power spectral density of jth component of the corrective process $f_j^C(t), (j = 1, 2, ..., m)$ can be determined using the recursive procedure proposed by [32]:

$$G_j^C(\omega) = 0 \quad 0 \leq \omega \leq \omega_{lc}, \tag{14}$$

$$G_j^C(\omega_i) = \frac{4\zeta_0}{\omega_i \pi - 4\zeta_0 \omega_{i-1}} \left(\frac{(RSA^j(\omega_i,\zeta_0))^2 - (RSA^{f_j^L}(\omega_i,\zeta_0))^2}{(\eta_{U^C}(\omega_i,\zeta_0))^2} \right.$$
$$\left. - \Delta\omega \sum_{r=1}^{i-1} G_j^C(\omega_r) \right), \tag{15}$$
$$\omega_{lc} \leq \omega \leq \omega_C, \quad \omega_i = \omega_{lc} + i\Delta\omega$$

$$\eta_{U^C}^{(j)}(\omega_i,\zeta_0,T_s,P=0.5) = \sqrt{2\ln\{2N_{U^C}^{(j)}[1-\exp[-(\delta_{U^C}^{(j)})^2\sqrt{\pi\ln(2N_{U^C}^{(j)})}]]\}} \tag{16}$$

$$N_{U^C}^{(j)} = \frac{T_s}{2\pi}\omega_i(-\ln p)^{-1} \tag{17}$$

$$\delta_{U^C}^{(j)} = \left[1 - \frac{1}{1-\zeta_0}\left(1 - \frac{2}{\pi}\arctan\frac{\zeta_0}{\sqrt{1-\zeta_0}}\right)^2\right]^{1/2} \tag{18}$$

where, $\eta_{U^c}^{(j)}$ is the peak factor, ζ_0 is the damping ratio, T_s is the duration of observing window set equal to the strong motion phase of the process $f_j^L(t)$, $\omega_{lc} \cong 1$ rad/s is the lowest bound in the domain of η_{U^C}. The accuracy of the power spectral density of each individual corrective term can be iteratively improved via the equation:

$$G_j^C(\omega)_K = G_j^C(\omega)_{k-1}\left[\frac{(RSA^{(j)}(\omega,\zeta_0))^2}{(RSA^{f_j^L}(\omega,\zeta_0) + (RSA^{f_j^C}(\omega,\zeta_0))^2)_{k-1}}\right] \tag{19}$$

where, $(RSA^{f^C}(\omega,\zeta_0))_k$ represents the response spectrum of the corrective term determined at the kth iteration; $(RSA^{(j)}(\omega,\zeta_0))$ is the jth target response spectrum and; $(RSA^{f^L}(\omega,\zeta_0))$ is the scaled response spectrum of the local component. The iteration is terminated when:

$$\left|\frac{RSA^j(\omega) - RSA^{f_j^{SC}}(\omega)}{RSA^j(\omega)}\right| \leq \varepsilon, \tag{20}$$
$$\forall \omega_l \leq \omega \leq \omega_u \quad (j = 1, 2, ..., m)$$

where, $RSA^{f_j^{SC}}(\omega)$ is the jth ensemble averaged response spectrum of the simulated ground motion vector process. For each iteration, the response spectra , $RSA^{f_j^{SC}}(\omega)$ $(j = 1, 2, ..., m)$

which can be determined approximately by methods presented in [33], [34].

2.3 Fully Non-Stationary and Spectrum-Compatible Sample Function

After determining the PSD of the corrective term, the elements of the evolutionary spectrum-compatible cross-spectral density matrix, $S^{SC}(\omega,t)$ are established as follows:

$$S_j^C(\omega) = 0.5G_j^C(\omega) \tag{21}$$

$$S_j^C(\omega,t) = \varphi_j^2(t)S_j^C(\omega), \quad (j = 1, 2, ..., m) \tag{22}$$

$$\varphi(t) = \begin{cases} \left(\dfrac{t}{t_1}\right) & t < t_1 \\ 1 & t_1 \leq t \leq t_2 \\ \exp[-\beta(t-t_1)] & t > t_2 \end{cases} \tag{23}$$

when, t_1 and t_2 are the time instant when $E_L^{(j)}$ (Husid Function) assumes the values of 0.05 and 0.95 and; $\beta = 0.1734 s^{-1}$. It should be noted that $T_s = t_2 - t_1$ must satisfy the limit imposed by the code $T_s \geq 10s$ [35]. After determining the power spectral density function of the corrective term Eq. (22), the element of evolutionary spectrum-compatible cross-spectral density matrix $S_j^{SC}(\omega,t)$ are established as follow:

$$S_{jj}^{SC}(\omega,t) = S_{jj}^L(\omega,t) + S_{jj}^C(\omega,t), \quad j = 1, 2, .., m \tag{24}$$

$$S_{jk}^{SC}(\omega,t) = \sqrt{S_{jj}^{SC}(\omega,t)S_{kk}^{SC}(\omega,t)}\Gamma_{jk}(\omega),$$
$$j, k = 1, 2, ..., m \tag{25}$$

where, $S_j^{LL}(\omega,t)$ is power spectral density of the local component and $\Gamma_{jk}(\omega)$ is the complex coherency function. Finally, after computing the elements of evolutionary spectrum-compatible cross-spectral density matrix, the fully non-stationary ground motion time history ($f_j^{sc}(t), (j = 1, 2, ..., m)$) that reflect a prescribe response spectrum can be generated through Eq. (10) to Eq. (13). The flow chart shown in Fig. 1 reveals the steps of calculating fully non-stationary ground motion time history.
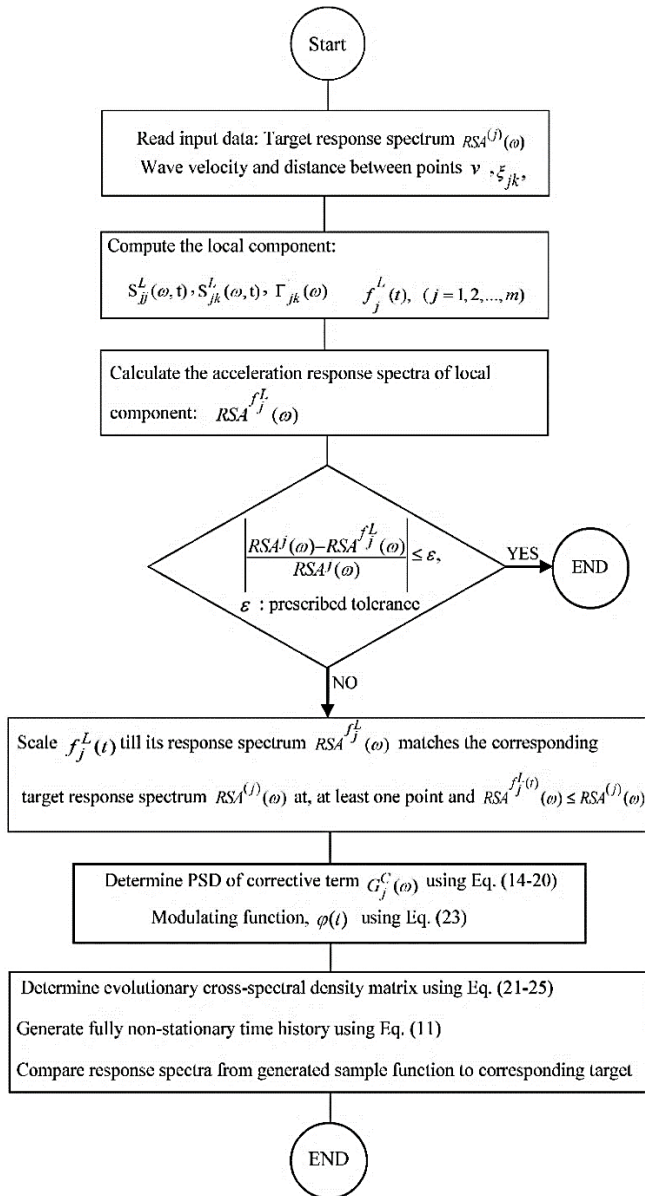
Fig. 1: Flow chart of the proposed methodology for generating ground motion

3. Finite Element Modeling of a Series of Typical Arch Dams

3.1 Dam Shape Geometric Properties

The current study considers the horizontal curves of the upstream and downstream as parabolic. Supplementary information used to form the dam body shape can be found in[36]. The models are developed in U-shaped and V-shaped valleys for two different heights of 150m and 250m. Table 1 exhibits other geometric properties.

3.2 Structural-Material Properties and Boundary Conditions

Finite element models of typical arch dams are provided to investigate how the chosen coherency functions affect the

stresses magnitudes and distributions within the dam body. This is one of the novelties in the current study, in which several finite element models of high arch dams having specific characteristics are provided. Moreover, the study is not limited to a model with predefined geometry. In this regard, four different finite element models of V-shaped and U-shaped valleys having 150m and 250m heights (see Fig. 2) are also considered to study the effect of dam body shape on stress distribution patterns and magnitudes.

Table 1: Geometric properties of considered dam body shapes

Property	Height 250	
	U-shaped	V-shaped
Valley width at crest level	750m	750m
Valley width at base level	350m	150m
Abutment slope	0.8	1.2
Body thickness at Crest	12m	12m
Body thickness at Base	69m	58m
Body thickness at $0.6 \times$ height	39m	34m
Body thickness at $0.3 \times$ height	66m	55m
Body Shape	symmetric	

Property	Height 150	
	U-shaped	V-shaped
Valley width at crest level	450m	450m
Valley width at base level	270m	90m
Abutment slope	0.7	1.2
Body thickness at Crest	7m	7m
Body thickness at Base	30m	23m
Body thickness at $0.6 \times$ height	18m	15m
Body thickness at $0.3 \times$ height	29m	22m
Body Shape	symmetric	

The length of the reservoir at the upstream of the dam body is equal to the foundation finite element model extension in the upstream direction for all finite element models to consider the fluid-structure interaction on both the dam body's upstream face and the reservoir interface with it's surrounding sides. Due to the relatively low ratio of the modulus of deformation of the rock mass to the mass concrete's elastic modulus, the surrounding foundation rock finite element model is extended about three times the dam height in all directions. The foundation rock is continuous up to higher elevations from the dam crest to simulate the sites' real abutment conditions. The dam body and surrounding rock foundation are modeled using 8-node

SOLID elements having three translational degrees of freedom at each node. The reservoir medium is modeled using 8-node Eulerian fluid elements, with pressure as the degree of freedom at each node. The number of elements used to model the dam body, foundation rock, and the reservoir is 640, 11520, and 2560 elements, respectively. Hydrodynamic pressure at the free surface of the reservoir is set to be zero (neglecting surface waves), and the Sommerfeld condition is applied on the far end truncated boundary of the reservoir to model full absorption of the outgoing waves (read details in [37]).

To simulate semi-infinite condition, far-end boundaries of the surrounding foundation rock are selected and the viscous dampers are applied on the relevant areas to absorb outgoing waves and prevent wave reflection into the finite element model of the foundation (see details in[37]).The modulus of elasticity, Poisson's ratio and density for the mass concrete are 30GPa, 0.2, 2400kg/m^3, respectively. The value of 11.5Gpa is taken as the modulus of deformation of the surrounding foundation rock and its Poisson's ratio and density are 0.25 and 2000kg/m^3, respectively. The wave reflection coefficient due to sedimentation at the bottom of the reservoir and the sound velocity in water are taken as 0.8 [38]and 1436m/s, respectively. The concrete damping ratio is assumed to be 5% [39]and this value for the surrounding rock mass is taken as 2%. The mass and stiffness proportional damping values are calculated using the formulation proposed by [40] corresponding to natural vibration frequencies of 2Hz and 6Hz for the structure.
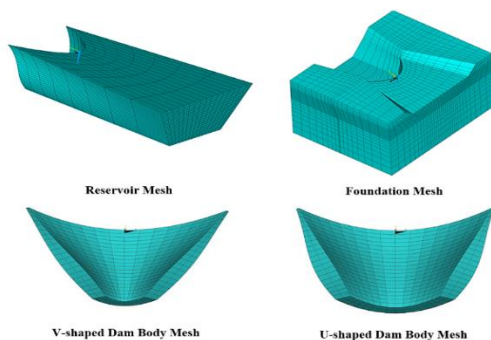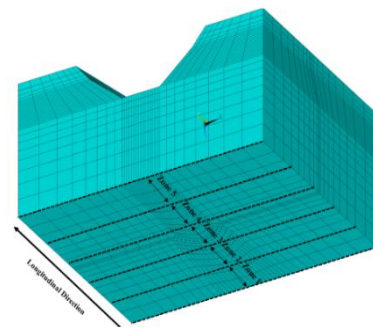
occurred displacements are set to zero, and the stresses are applied as the initial condition for the next step of loading. The normal water level is applied as a load step, and finally, the seismic excitation is imposed on the model. To generate non-uniform ground motions, the wave propagation velocity, station distances, and response spectrum of the local site are the three most significant inputs. As mentioned previously, the effect of wave passage is not considered in this study. Therefore, the wave velocity is selected to be infinite for eliminating the delay in arrival time to the stations (see EQ. 6). As can be seen in EQ. 6, the coherency will decay with the station separation, so the distance between stations is the second important component.

In the current study, in both the longitudinal and transverse directions, the distance between stations is extracted by dividing the foundation base into five partially equal zones (see Fig. 3). Each zone's central coordinate axis is selected as the station's location, and the generated non-uniform time histories are calculated by the coherency function and determinant spectral density matrix. Because of similar rock mass conditions, the target response spectrums are the same at five different stations, and the generated time histories are compatible with the target response spectrum. Figs. 4 and 5 compare the generated ground motion for sequential stations using two different (Harichandran-Vanmarcke and Hindy-Novak) coherency functions due to stream (longitudinal) direction wave propagation. The generated ground motions' response spectrum and the target one are shown in Fig. 6. As can be seen, the generated response spectra are in good agreement with the target ones.

Fig. 2: Finite element model of dam-reservoir-abutment
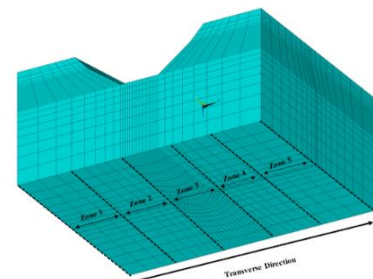
3.3 Sequential Loading

The self-weight of the surrounding rock mass and the dam body, the hydrostatic pressure in normal water level and then, the seismic excitation are applied as static and dynamic loads. For simulating the real condition, at first, the surrounding foundation and its boundary conditions are modeled and analyzed. Then, the displacements are set to zero, and the stresses are saved and applied as the initial condition for the next load step. In the second step, the dam body self-weight is applied, and as previously executed, the

(a)Propagation in upstream-downstream (longitudinal) direction
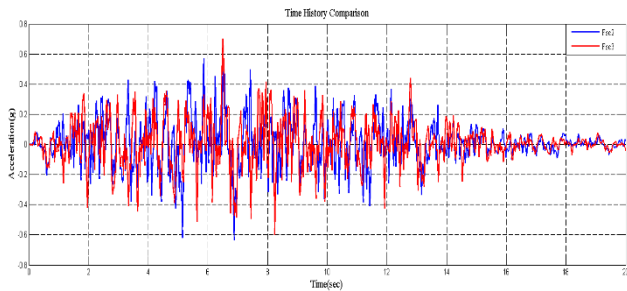

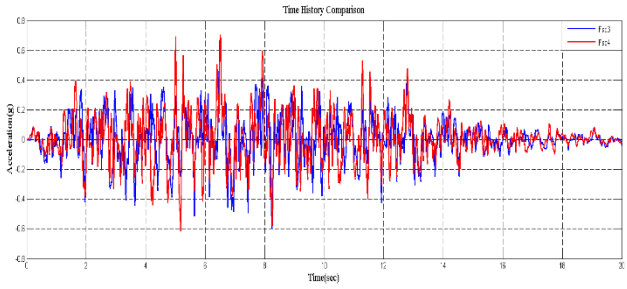(b) Propagation in cross stream (transverse) direction
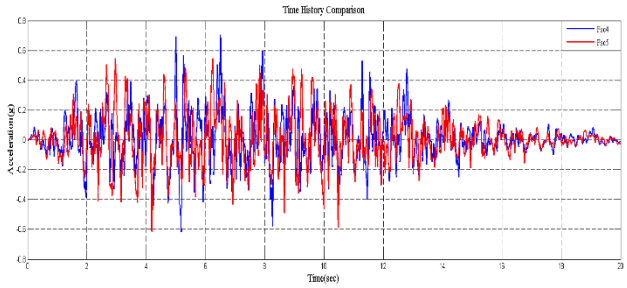**Fig. 3:** Wave propagation direction
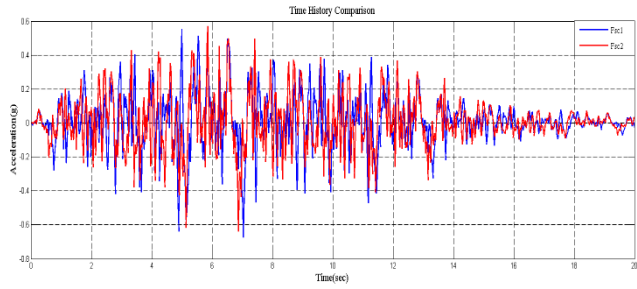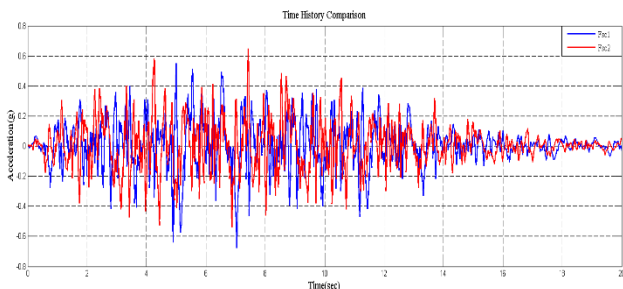
(a) stations 1 vs 2

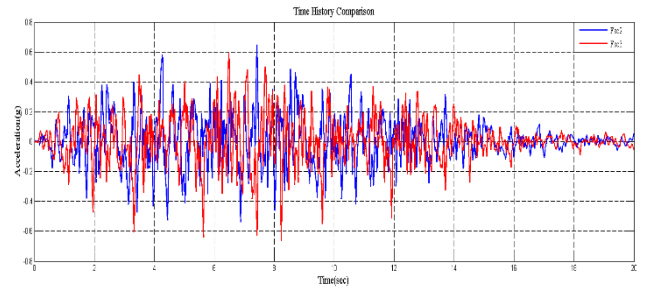

(b) stations 2 vs 3

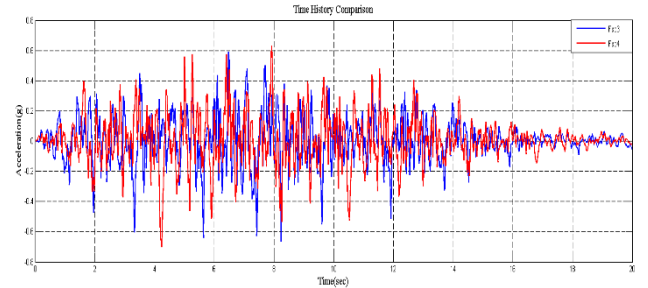(c) stations 3 vs 4

(c) stations 4 vs 5

Fig. 4: Comparison of generated time histories for the sequential points; Stream direction;Harichandran-Vanmarcke coherency function
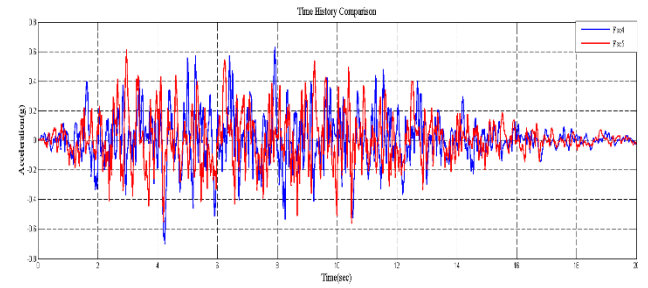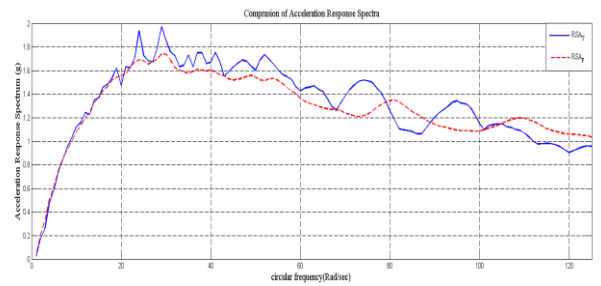

(a) stations 1 vs 2

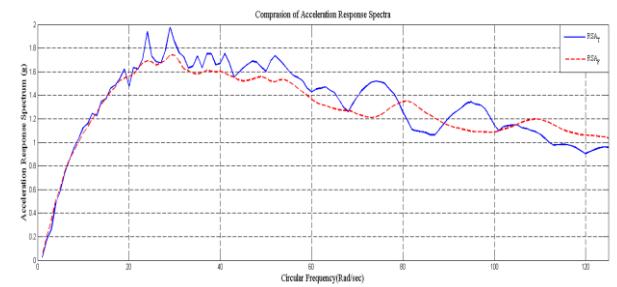(b) stations 2 vs 3

(c) stations 3 vs 4

(c) stations 4 vs 5

Fig. 5: Comparison of generated time histories for the sequential points; Stream direction; Hindy-Novak coherency function

(a) Harichandran-Vanmarcke coherency function

(b) Hindy-Novak coherency function

Fig. 6: Comparison of generated time histories response spectrum with the target one

4. Results and Discussion

In this section, the effects of SVEGM on stress distribution patterns and their maximum values are studied considering two different mentioned coherency functions. Ground motions are applied in longitudinal (stream) and transverse directions separately, at five different determined zones on the foundation (see Fig. 3). Maximum tensile and compressive non-current principal stress envelopes are obtained, applying both the static and dynamic loads.

4.1 Stress Envelopes for Dam Body Having 250m Height

4.1.1 Stresses Due to Cross stream Wave Propagation

Figs. 7 and 8 show non-concurrent envelopes of the first and third principal stresses experienced on the upstream and downstream faces.
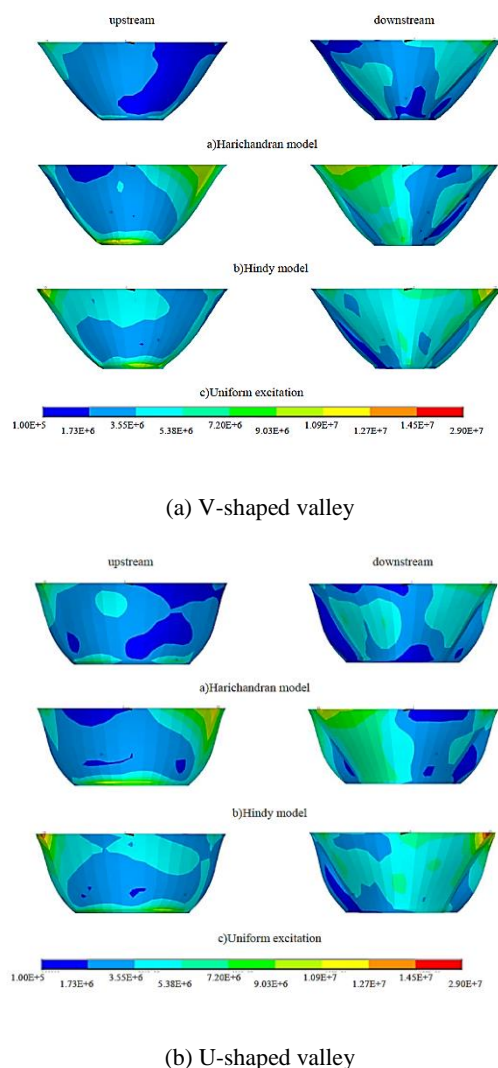

(a) V-shaped valley

(b) U-shaped valley

Fig. 7: Non-concurrent envelope of the first principal stress; cross-stream wave propagation; 250m dam body height (in P a)

Comparing results from figure 7 reveals that in both conditions, maximum stresses occur in the vicinity of the crest (on the left or right side of the body). Besides, the maximum value of stresses due to uniform excitation is greater than that of the non-uniform one. It is evident from figures that, in non-uniform excitation, the chosen coherency function can alter the stress distribution pattern. As can be seen, due to Harichandran-Vanmarcke coherency function, the highest stresses are developed in the left abutment and near the crest. But, for Hindy-Novak coherency function, the highest stresses occur at the right side of the dam body in the vicinity of the crest and the middle, close to the bottom of the dam body. Moreover, comparing magnitudes of stresses reveals that, Hindy-Novak coherency function yields a greater value of the highest tensile principal stress than Harichandran-Vanmarcke model.

Investigating the effect of geometrical shapes (V-shaped vs. U-shaped) of the dam body shows that the stress distribution patterns under uniform and non-uniform excitations are close together. However, the tensile stress's maximum value is smaller for the V-shaped valley in all excitation conditions.

Figure 8 shows that results are similar to the first principal stress envelope, which means the maximum stresses occur at the crest level. For uniform excitations, the maximum values are concentrated in the middle of the crest. Numerical values of maximum compressive stresses in uniform excitations are greater than those obtained from nonuniform ones except in the U-shaped valley due to the HindyNovak coherency function. Due to applying various coherency functions, stress distribution patterns vary. Utilizing Harichandran-Vanmarcke coherency function, higher values of stresses occur approximately at the dam's right side near the crest. However, the Hindy-Novak coherency function leads to higher stress values on the left side of the crest. Besides, Harichandran-Vanmarcke coherency function causes greater amount of compressive stresses.

Concerning the effect of valley shape on the compressive stresses in both geometrical shapes, the stress distribution patterns are very similar for all excitation conditions, meaning the patterns are not affected by geometry shapes. However, the effect of the geometry shape on magnitudes of stresses depends on the coherency function.
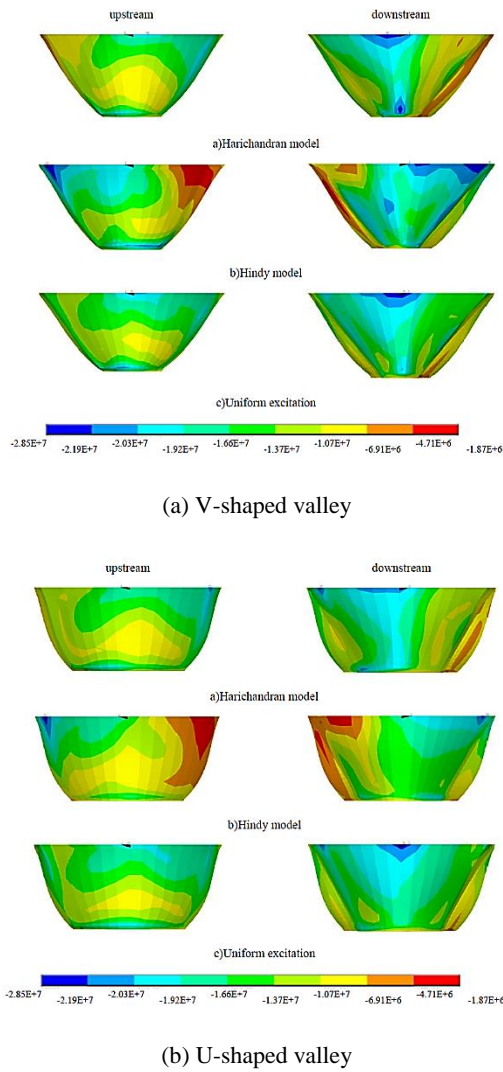
(a) V-shaped valley

(b) U-shaped valley

Fig. 8: Non-concurrent envelope of the third principal stress; cross stream wave propagation; 250m dam body height (in P a)

4.1.2 Stresses Due to Stream Wave Propagation

Figs. 9 and 10 represent non-concurrent envelopes of the first and third principal stresses due to excitation in the stream (longitudinal) direction.

Focusing on Fig. 9, it is found that for both uniform and non-uniform excitations, high-stress contours occur along the crest and a small region near the bottom of the dam body. Also, under uniform ground motions, the regions with high stresses are in the middle of the dam crest.

Similar to cross stream wave propagation, the maximum value of the tensile stress is higher in the cases under uniform excitations. Concerning the effect of coherency functions, it can be seen that contrary to cross-stream direction, stress distributions are similar for both coherency models.

The maximum value of tensile stress caused by the Harichandran-Vanmarcke coherency function is greater in comparison with that obtained from Hindy-Novak. The geometrical shape of the dam has no effect on the distribution pattern for the first principal stress, while comparing the magnitude of stresses reveals that, the maximum tensile stress in the V-shaped valley is lower than that obtained for the U-shaped body.
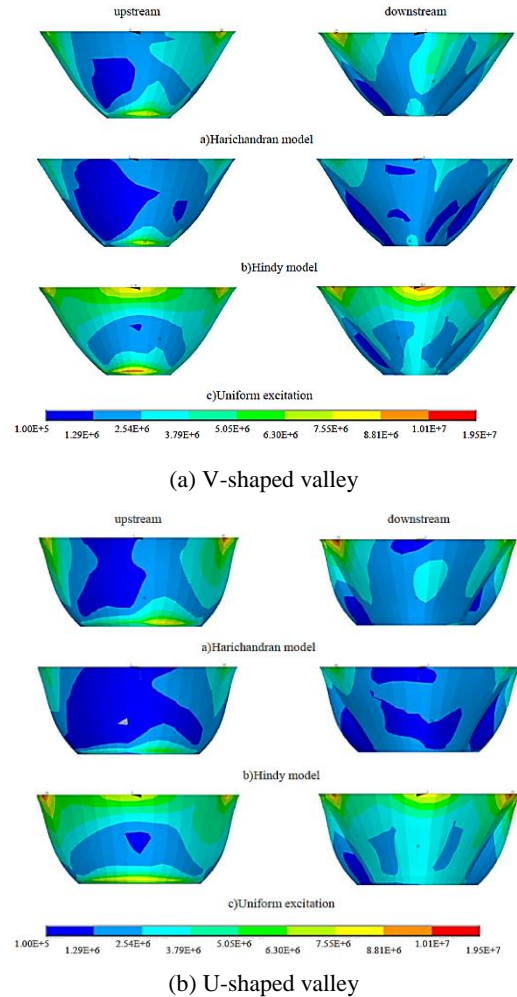

(a) V-shaped valley

(b) U-shaped valley

Fig. 9: Non-concurrent envelope of the first principal stress; stream wave propagation; 250m dam body height (in P a)

Considering Fig. 10, under uniform and non-uniform excitations, as well as both coherency functions, the stress distributions are similar and generate symmetric patterns. Moreover, the maximum compressive stresses occur in the middle of the crest.

The maximum value produced by uniform excitations is greater than those obtained in non-uniform ones. Furthermore, for both geometrical shapes the stress distribution patterns are considerably close. Furthermore, in all excitation conditions, the maximum value of the stresses for the U-shaped valley is greater than those obtained for the V-shaped ones.
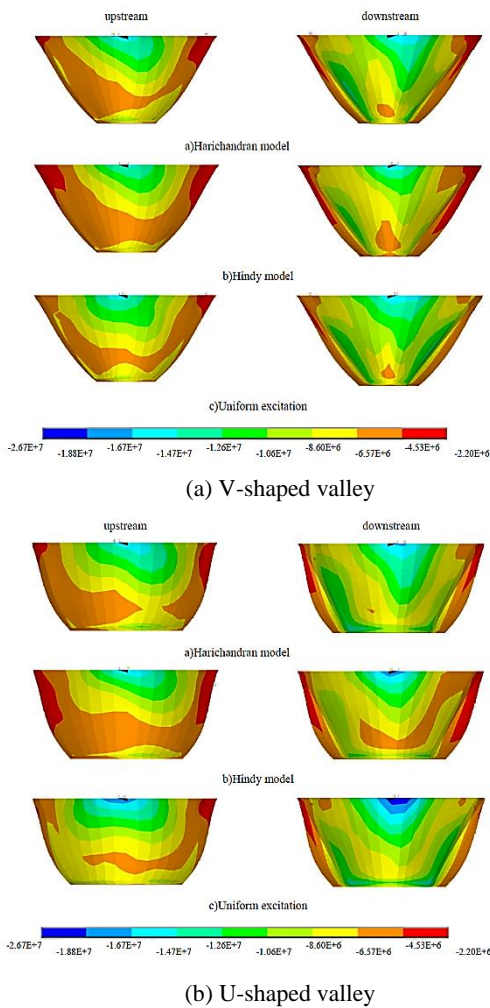
(a) V-shaped valley

(b) U-shaped valley

Fig. 10: Non-concurrent envelope of the third principal stress; stream wave propagation; 250m dam body height (in Pa)

4.2 Stress Envelopes for Dam Body Having 150m Height

4.2.1 Stresses Due to Cross stream Wave Propagation

As done in previous subsections, Figs. 11 and 12 represent non-current envelopes of the first and third principal stresses on the upstream and downstream faces.

Comparing uniform with non-uniform ground motions, it is obvious that the maximum stress occurs at the crest region or near the abutment in both excitation conditions. Moreover, the uniform excitation yields greater tensile stresses.

As seen from the figures, considering two coherency models, the stress distribution patterns are different. The region with the maximum value of the first principal stress due to the Hindy-Novak coherency function occurs near the crest. In contrast, for the Harichandran-Vanmarcke one, this region is situated near the abutment.

Concerning the effect of coherency function on the magnitudes of stresses, the maximum tensile stress is greater

when the Harichandran-Vanmarcke coherency function is used. The geometrical shape of the dam body seems not to be very influential in stress distribution patterns. The first principal stress's highest value is lower in the V-shaped body for uniform ground motions and non-uniform ground motions considering the Hindy-Novak coherency function.
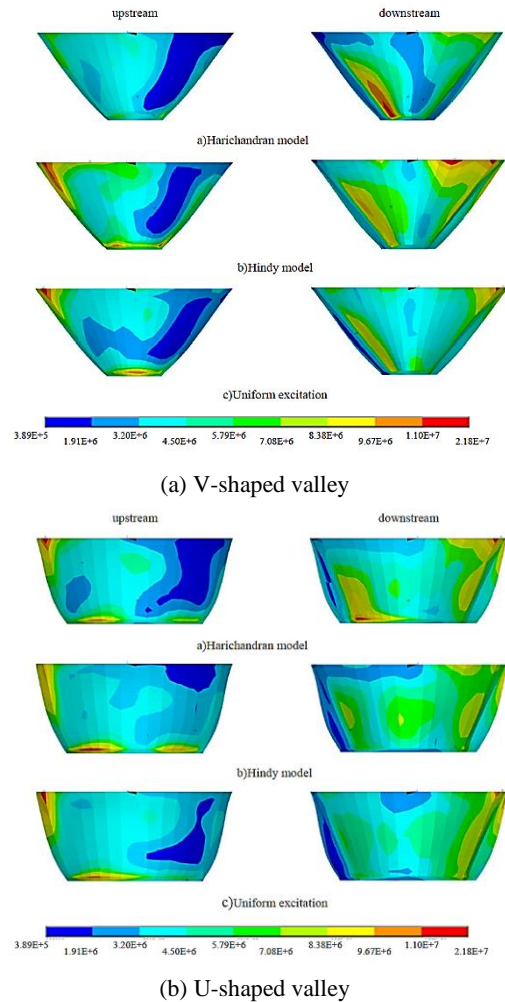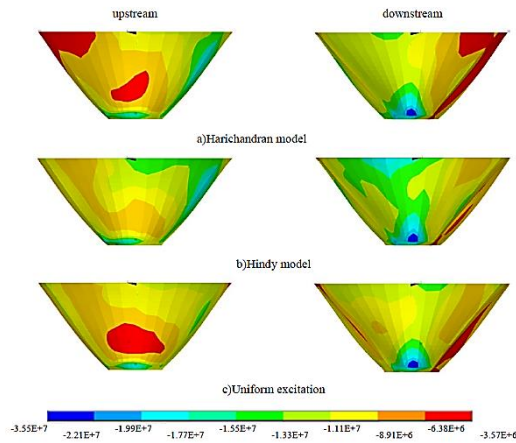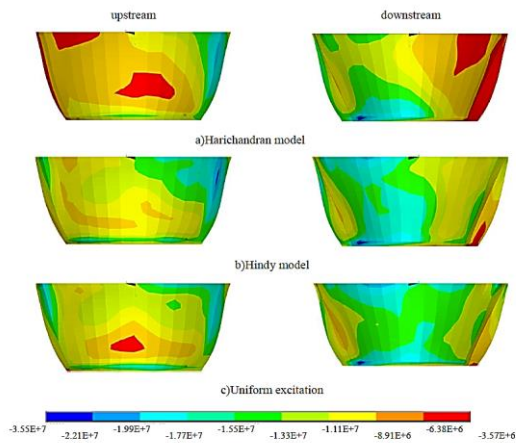

(a) V-shaped valley

(b) U-shaped valley

Fig. 11: Non-concurrent envelope of the first principal stress; cross stream wave propagation; 150m dam body height (in P a)

As shown in Fig. 12, compressive stress distribution patterns are similar for uniform and non-uniform excitation conditions for both coherency models, and the highest third principal stresses occur near the base. The maximum third principal stress due to uniform excitation is greater than the Hindy-Novak coherency function's value results.

Investigating the coherency model's effect reveals that the value of third principal stress using the Harichandran-Vanmarcke coherency function is greater than the Hindy-Novak one. Considering the effect of valley shape demonstrated that the third principal stress distribution patterns are extremely close, and are not affected by dam body shape. Again, the amount of highest third principal stress (compressive stress) in the V-shape body is greater than the U-shaped one in all excitation conditions.
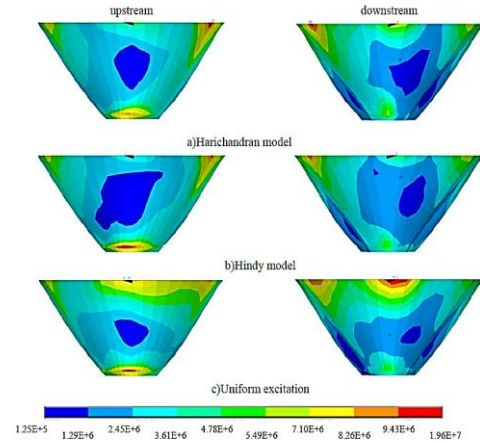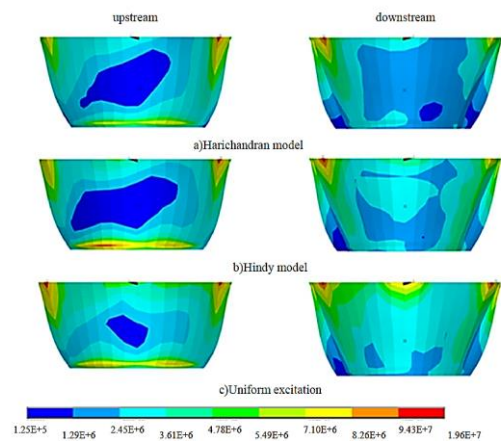
(a) V-shaped valley

(b) U-shaped valley

Fig. 12: Non-concurrent envelope of the third principal stress; cross stream wave propagation; 150m dam body height (in Pa)

(a) V-shaped valley

(b) U-shaped valley

Fig. 13: Non-concurrent envelope of the first principal stress; stream wave propagation; 150*m* dam body height (in *Pa*)
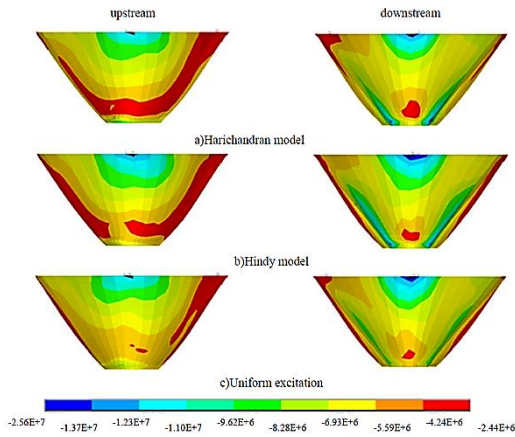
4.2.2 Stresses Due to Stream Wave Propagation

At last, Figs. 13 and 14 show the non-concurrent envelope of the first principal stress when the seismic wave propagates in the stream direction.

Comparing uniform and non-uniform cases of excitations, stress patterns are similar, but the region with higher stresses is wider due to uniform ground motions. The maximum tensile stress resulting from the uniform excitation is greater than this value when using the Hindy-Novak coherency model and smaller than the value when using the Harichandran-Vanmarcke coherency function.

Regarding the effect of coherency models, stress distribution patterns are not considerably disparate. However, the areas experiencing greater tensile stresses are broad when using the Harichandran-Vanmarcke model. Moreover, Harichandran-Vanmarcke coherency function creates greater value. Again, it is manifested that that stress distribution patterns are not affected by the valley shape. Examining two body shapes, the dam body's maximum tensile stress is lower in the V-shaped valley as expected.

Considering the third principal stress from Fig. 14, it is found that the regions with higher compressive stress intensity are more distributed when the dam excited with a uniform model beside it yields greater maximum compressive stress. Regarding the effect of coherency models, the regions with higher stresses are more expansive when using the Hindy-Novak coherency function. But, Harichandran-Vanmarck coherency model creates greater values. Finally, by examining the body shapes, it becomes more obvious that stress distribution patterns are close. The maximum value of the stresses is lower in the V-shaped body for all excitation conditions.
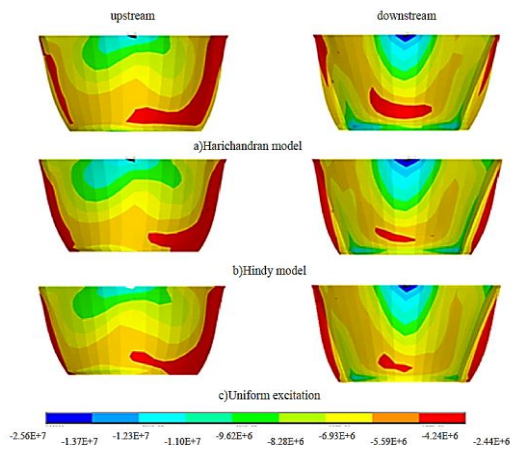
(a) V-shaped valley

(b) U-shaped valley

Fig. 14: Non-concurrent envelope of the third principal stress; stream wave propagation; 150*m* dam body height (in *Pa*)

5. Discussion on the Results

Generally, in the phase of analysis and design of a high arch dam, it is assumed that the mass concrete behaves linearly. In this phase of the study, contraction joints are not modeled. So, generating tensile stresses along the crest is expected. When seismic evaluation of an existing dam is the main subject of a study, modeling contraction joints and simulating nonlinear behavior of mass concrete utilizing an appropriate model is mandatory. In the current study, the main issue is investigating the structural effects of non-uniform excitations generated using various coherency functions. Thus, the dam body is assumed to behave as a linear elastic monolith block. In this space, the main parameters for evaluating the dam body behavior are the first and third principal stresses. In the previous subsections, stress distribution patterns resulted from conducted analyses were considered comprehensively. Tables 2, 3, 4, and 5 present a summary of stress results.

Table 2. Summary of Results- Maximum Tensile Stresses- Dam having 250m height

| Coherency function | Valley | Tensile Stress (MPa) | |
		Cross Stream	Stream
Harichandran-Vanmarcke	U-shape	16.3	**19.5**
	V-shape	15.4	**15.8**
Hindy-Novak	U-shape	22.2	**11.3**
	V-shape	20.9	**12.9**
No Coherency (uniform)	U-shape	28.9	**18.7**
	V-shape	22.5	**17.3**

Focusing on the above-referred tables, it is found that the maximum tensile and compressive stresses are higher in the U-shaped dam body as a general trend. However, there are some exceptions. Also, non-uniform excitation leads to less maximum tensile stress in comparison with the cases excited uniformly. Again, this is a general trend, and we can see some exceptions.

Table 3. Summary of Results- Maximum Compressive Stresses- Dam having 250m height

| Coherency function | Valley | Compressive Stress (MPa) | |
		Cross Stream	Stream
Harichandran Vanmarcke	U-shape	26.7	22.3
	V-shape	27.2	21.9
Hindy-Novak	U-shape	28.4	23.7
	V-shape	22.3	20.8
No Coherency (uniform)	U-shape	27.2	26.7
	V-shape	27.2	21.4

Table 4. Summary of Results- Maximum Tensile Stresses- Dam having 150m height

| Coherency function | Valley | Tensile Stress (MPa) | |
		Cross Stream	Stream
Harichandran Vanmarcke	U-shape	16.9	19.6
	V-shape	20.8	16.4
Hindy-Novak	U-shape	16.2	10.6
	V-shape	12.3	10.6
No Coherency (uniform)	U-shape	21.8	13.7
	V-shape	20.4	13.2

Table 5. Summary of Results- Maximum Compressive Stresses- Dam having 150m height

Coherency function	Valley	Compressive Stress (MPa)	
		Cross Stream	Stream
Harichandran Vanmarcke	U-shape	42.5	24.1
	V-shape	45.5	22.1
Hindy-Novak	U-shape	24.3	19.1
	V-shape	28.8	15.0
No Coherency (uniform)	U-shape	29.0	25.6
	V-shape	34.7	24.2

6. Conclusions

In this paper, the effects of spatially varying earthquake ground motions SVEGM on the stress distributions in four different typical arch dams were investigated, focusing on incoherency effects. Harichandran-Vanmarcke and Hindy-Novak coherency functions were utilized, and non-uniform spectrum-compatible ground motions were generated. Uniform and non-uniform simulated ground motions were applied at the stream and cross-stream directions, separately. The reservoir was assumed to be compressible, and the massed foundation surrounding the dam body was extended to an appropriate distance from the dam body. There were several findings presented in the previous sections in detail. Briefly, it can be said:

- Critical regions, where the greater value of stress occurs, for all excitation conditions, the highest stress manifests along the crest on the right or left side of the dam body, although all patterns are not the same.

- In terms of uniform and non-uniform excitation, uniform excitation yields a higher magnitude of stress than the non-uniform one. It confirms that dynamic analysis and design utilizing uniform excitation give conservative results.

- The stress distribution pattern is mainly affected by the chosen coherency function, depending on the excitation direction. When exciting in the cross-stream direction, the patterns are entirely different for both tensile and compressive stresses. But, when exciting in the stream direction, stress distribution patterns were relatively symmetric.

- The geometrical shape of the dam body does not influence the stress distribution patterns. However, it can change the magnitude of the stresses as shown, where the magnitude of maximum principal stress was generally lower in the V-shaped valley. Regarding international guides like USACE and USBR, it is expected that V-shaped arch dams give smoother stress

contours with fewer peak stresses as presented theoretically.

- Due to uniform excitation, as the dam height rises, the magnitude of the first principal stress (tensile component) increases, whereas the compressive components decrease. However, through non-uniform excitation, this trend depends on the selected coherency function.

Even though the spatial variation of earthquake ground motions and the effect on the response of extended structures has attracted significant consideration for nearly half a century, this phenomenon and its probable impact are still unknown because there are many uncertain and influential factors. In this case, the necessity of further complementary study is indisputable. In this case, future research could continue to explore the effect of various site conditions, the angle of incident waves, considering different coherence coefficients, examining the assumption of modeling the structures (linear and nonlinear analysis, boundary conditions, soil-structure interactions, structural details) and conditional simulation of non-uniform excitation in comparison with unconditional simulation.

References

[1] Salamon, J., et al., *Seismic assessment of a dam-foundation-reservoir system using Endurance Time Analysis*. 2019.

[2] Maheri, M. and H. Ghaffar-Zadeh, *Asynchronous and non-uniform support excitation analysis of large structures*. Journal of Seismology and Earthquake Engineering, 2002. 4(2-3): p. 63.

[3] Harichandran, R.S., *Spatial variation of earthquake ground motion, what is it, how do we model it, and what are its engineering implications*. Dept. of Civil and Environmental Engineering, Michigan State Univ., East Lansing, Mich, 1999.

[4] Chopra, A.K. and J.T. Wang, *Earthquake response of arch dams to spatially varying ground motion*. Earthquake Engineering & Structural Dynamics, 2010. 39(8): p. 887-906.

[5] Chopra, A.K., *Dynamics of structures: theory and applications to earthquake engineering*. 1995: Prentice Hall.

[6] Huang, J. and A. Zerva, *Earthquake performance assessment of concrete gravity dams subjected to spatially varying seismic ground motions*. Structure and infrastructure engineering, 2014. 10(8): p. 1011-1026.

[7] Alves, S.W., *Nonlinear analysis of Pacoima Dam with spatially nonuniform ground motion*. 2005, California Institute of Technology.

[8] Mirzabozorg, H., M. Akbari, and M.H. Ardebili, *Wave passage and incoherency effects on seismic response of high arch dams*. Earthquake Engineering and Engineering Vibration, 2012. 11(4): p. 567-578.

[9] Davoodi, M., M.K. Jafari, and S.M.A. Sadrolddini, *Effect of multi-support excitation on seismic response of embankment dams*. International Journal of Civil Engineering, 2013. 11(1): p. 19-28.

[10] Yao, Y., et al., *Seismic response of high concrete face rockfill dams subjected to non-uniform input motion*. Acta Geotechnica, 2019. 14(1): p. 83-100.

[11] Davoodi, M., A. Razmkhah, and A. Javaheri, *Considering the effects of SVEGM on dynamic stress-strain distribution of embankment dams*. Civil Engineering Infrastructures Journal, 2012. 45(5): p. 529-541.

[12] Sohrabi-Gilani, M. and M. Ghaemian, *Spatial variation input effects on seismic response of arch dams.* Scientia Iranica, 2012. 19(4): p. 997-1004.

[13] Bilici, Y., et al., *Stochastic dynamic response of dam–reservoir–foundation systems to spatially varying earthquake ground motions.* Soil Dynamics and Earthquake Engineering, 2009. 29(3): p. 444-458.

[14] Falamarz-Sheikhabadi, M. and A. Zerva, *Two uncertainties in simulating spatially varying seismic ground motions: incoherency coefficient and apparent propagation velocity.* Bulletin of Earthquake Engineering, 2018. 16(10): p. 4427-4441.

[15] Zerva, A., M.R. Falamarz-Sheikhabadi, and M.K. Poul. *Issues with the use of spatially variable seismic ground motions in engineering applications.* in *European Conference on Earthquake Engineering Thessaloniki, Greece.* 2018. Springer.

[16] Adanur, S., et al., *Wave-passage effect on the seismic response of suspension bridges considering local soil conditions.* International Journal of Steel Structures, 2017. 17(2): p. 501-513.

[17] Bayraktar, A., K. Haciefendioglu, and M. Muvafik, *Asynchronous seismic analysis of concrete-faced rockfill dams including dam–reservoir interaction.* Canadian Journal of Civil Engineering, 2005. 32(5): p. 940-947.

[18] Wang, D., et al., *Wave-Passage Effect of Earthquake Loadings on Long Structures.* International Journal of Structural Stability and Dynamics, 2016. 16(07): p. 1550037.

[19] Xiong, M., Y. Huang, and Q. Zhao, *Effect of travelling waves on stochastic seismic response and dynamic reliability of a long-span bridge on soft soil.* Bulletin of Earthquake Engineering, 2018. 16(9): p. 3721-3738.

[20] Zhang, Y., et al., *Wave passage effect of seismic ground motions on the response of multiply supported structures.* Structural Engineering and Mechanics, 2005. 20(6): p. 655-672.

[21] Chen, M.-T. and R.S. Harichandran, *Response of an earth dam to spatially varying earthquake ground motion.* Journal of Engineering Mechanics, 2001. 127(9): p. 932-939.

[22] Cacciola, P. and G. Deodatis, *A method for generating fully non-stationary and spectrum-compatible ground motion vector processes.* Soil Dynamics and Earthquake Engineering, 2011. 31(3): p. 351-360.

[23] Deodatis, G., *Simulation of ergodic multivariate stochastic processes.* Journal of engineering mechanics, 1996. 122(8): p. 778-787.

[24] Hao, H., C. Oliveira, and J. Penzien, *Multiple-station ground motion processing and simulation based on SMART-1 array data.* Nuclear Engineering and Design, 1989. 111(3): p. 293-310.

[25] Shinozuka, M. and G. Deodatis, *Simulation of stochastic processes by spectral representation.* Applied Mechanics Reviews, 1991. 44(4): p. 191-204.

[26] Wang, J., et al., *Simulations of non-stationary frequency content and its importance to seismic assessment of structures.* Earthquake engineering & structural dynamics, 2002. **31**(4): p. 993-1005.

[27] Clough, R.W. and J. Penzien, *Structural dynamics.* New York: McGrowHill Inc, 1975.

[28] Bogdanoff, J.L., J.E. Goldberg, and M. Bernard, *Response of a simple structure to a random earthquake-type disturbance.* Bulletin of the Seismological Society of America, 1961. 51(2): p. 293-310.

[29] Zerva, A., *Spatial variation of seismic ground motions: modeling and engineering applications.* 2016: Crc Press.

[30] Harichandran, R.S. and E.H. Vanmarcke, *Stochastic variation of earthquake ground motion in space and time.* Journal of Engineering Mechanics, 1986. 112(2): p. 154-174.

[31] Hindy, A. and M. Novak, *Pipeline response to random ground motion.* Journal of the Engineering Mechanics Division, 1980. 106(2): p. 339-360.

[32] Cacciola, P., *A stochastic approach for generating spectrum compatible fully nonstationary earthquakes.* Computers & Structures, 2010. 88(15-16): p. 889-901.

[33] Rosenblueth, E., *basis for aseismic design of structures.* 1951.

[34] Vanmarcke, E. and D. Gasparini, *Simulated earthquake ground motions*, in *Structural mechanics in reactor technology.* 1977.

[35] Standard, B., *Eurocode 6—Design of masonry structures—.* British Standard Institution. London, 2005.

[36] Asaadi, A.R., et al., *Reshaping of a Double-Curvature Arch Dam Using APSO Algorithm to Increase Safety.* 2019.

[37] Mirzabozorg, H., M. Varmazyari, and S.A. Gharehbaghi, *Seismic evaluation of existing arch dams and massed foundation effects.* Soils and Foundations, 2016. 56(1): p. 19-32.

[38] Commission, F.E.R., *Engineering guidelines for the evaluation of hydropower projects .Chapter 11-Arch Dams.* 1999.

[39] Souri, A. and H. Mirzabozorg, *MATERIAL DAMPING EVALUATION IN A TYPICAL CONCRETE GRAVITY DAM.* INGEGNERIA SISMICA, 2018. 35(3): p. 121-138.

[40] Hall, J.F., *Problems encountered from the use (or misuse) of Rayleigh damping.* Earthquake engineering & structural dynamics, 2006. 35(5): p. 525-545.